Ocean Dynamics manuscript No.
(will be inserted by the editor)

A discontinuous finite element baroclinic marine model on unstructured prismatic meshes

Part II: implicit/explicit time discretization

Richard Comblen · Sébastien Blaise · Vincent Legat · Jean-François Remacle · Eric Deleersnijder · Jonathan Lambrechts

Revised peprint to be submitted to *Ocean Dynamics*
October, 2010

Abstract We describe the time discretization of a three-dimensional baroclinic finite element model for the hydrostatic Boussinesq equations based upon a Discontinuous Galerkin finite element method. On one hand, the time marching algorithm is based on an efficient mode splitting. To ensure compatibility between the barotropic and baroclinic modes in the splitting algorithm, we introduce Lagrange multipliers in the discrete formulation. On the other hand, the use of implicit-explicit Runge-Kutta methods enables us to treat stiff linear operators implicitly, while the rest of the nonlinear dynamics is treated explicitly. By way of illustration, the time evolution of the flow over a tall isolated seamount on the sphere is simulated. The seamount height is 90% of the mean sea depth. Vortex shedding and Taylor caps are observed. The simulation compares well with results published by other authors.

R. Comblen[a,b,c] · S. Blaise[a,b,c] · V. Legat[a,b,c] · J.-F. Remacle[a,b,c] · E. Deleersnijder[a,b,c,d] · J. Lambrechts[a,b,c]
Université catholique de Louvain,
[a] Institute of Mechanics, Materials and Civil Engineering (IMMC),
[b] Georges Lemaître Centre for Earth and Climate Research (TECLIM),
[c] Centre for systems engineering and applied mechanics (CESAME),
[d] Earth and Life Institute (ELI),
Euler, 4 Avenue G. Lemaître, B-1348 Louvain-la-Neuve, Belgium

S. Blaise
Currently at Institute for Mathematics Applied to Geosciences, National Center for Atmospheric Research, 1850 Table Mesa Drive, Boulder, CO 80305, USA.

1 Introduction

The spatially discretized ocean system is a dynamical system with a very large number of unknowns. It is the case for many computational fluid dynamics problems. However, oceanic problems typically consider very large time scales compared to those of the rapidly varying dynamics of local flows. Indeed, for climate modeling, centuries are considered, while it only takes a few hours for a surface gravity wave to propagate around the world.

Early models used the rigid-lid approximation, where the sea surface is assumed to be a rigid horizontal, impermeable boundary. This approximation filters out the fast surface gravity waves. The two-dimensional mean problem is solved either using a streamfunction formulation (Bryan, 1969) or a surface pressure formulation (Dukowicz et al., 1993). The computation of the surface pressure or streamfunction leads to elliptic two-dimensional problems, the rest of the dynamics being computed with explicit methods such as leap-frog with filtering (Griffies et al., 2000). Explicit methods for hyperbolic problems are subject to the Courant-Friedrichs-Lewy stability condition: the time step must be sufficiently small. The information in a cell only influences its direct neighbors, or the time step scales as the ratio of the grid size to the fastest wave speed. For rigid-lid models, the fastest phenomena are internal gravity waves. When free-surface is taken into account, much faster phenomena occur: surface gravity waves propagates roughly two orders of magnitude faster than internal gravity waves. Reducing the baroclinic time step by a factor of a hundred was not an option for the first free-surface models (Blumberg and Mellor, 1987; Killworth et al., 1991), and specific algorithms were designed to overcome this problem.

The purely explicit mode-splitting procedure, used in a large number of models (Kubatko et al., 2008), consists in integrating the two-dimensional barotropic equations with many explicit time steps while the three-dimensional baroclinic equations are solved with a single, much larger time step. For long term computations, the numerical model must be consistent by being able to advect a constant concentration of a given tracer exactly, up to machine accuracy. To achieve this so-called consistency requirement, the advection term of the tracer equation must degenerate to the continuity equation when a constant tracer concentration is considered (White et al., 2008). Compatibility between the two-dimensional and the three-dimensional approximations of the velocity field is also a mandatory requirement to ensure consistency (Deleersnijder, 1993). Therefore, the three-dimensional velocities are a posteriori corrected so that their averages match the velocities of the barotropic mode (Blumberg and Mellor, 1987), i.e. to obtain compatibility. Averaging in time the two-dimensional quantities in the three-dimensional dynamics is usually needed to ensure stability (Griffies et al., 2000; Higdon and de Szoeke, 1997; Hallberg, 1997).

To get rid of this a posteriori correction step of the three-dimensional velocities, the two-dimensional barotropic mode can be time stepped implicitly, using the same time step as the three-dimensional baroclinic mode (Dukowicz and Smith, 1994). Therefore, no correction step is needed, when all three-dimensional terms are advanced explicitly in time. The model will be both compatible and consistent, but the time step will be small. However, some terms in the three-dimensional momentum equation can be advanced implicitly in time, ifthose implicit terms have only a small influence on the two-dimensional barotropic mode (Wang, 2007).

An efficient strategy to discretize implicitly the free-surface equation is to solve a smaller system corresponding to the Schur complement of the system. If the linear

discrete system corresponding to the horizontal three-dimensional momentum and free-surface equations reads:

$$\begin{bmatrix} M_{\boldsymbol{u}} & G \\ D & M_\eta \end{bmatrix} \begin{bmatrix} X_{\boldsymbol{u}} \\ X_\eta \end{bmatrix} = \begin{bmatrix} F_{\boldsymbol{u}} \\ F_\eta \end{bmatrix},$$

where $M_{\boldsymbol{u}}$, M_η and $X_{\boldsymbol{u}}$, X_η are the mass matrices and vectors of degrees of freedom for velocities and elevation, respectively, G and D correspond to the elevation gradient term of the horizontal momentum equation and the velocity divergence term of the free-surface elevation equation, while $F_{\boldsymbol{u}}$ and F_η are their right-hand sides.

An equivalent smaller system for the elevation is obtained substituting $X_{\boldsymbol{u}}$ in the last line of the system:

$$\left[M_\eta - DM_{\boldsymbol{u}}^{-1}G\right] X_\eta = F_\eta - DM_{\boldsymbol{u}}^{-1}F_{\boldsymbol{u}}.$$

Such a methodology was used by Dukowicz and Smith (1994) as well as by Marshall et al. (1997) for global-scale models, but also by Giraldo et al. (2003) for shallow water problems on the sphere. Discontinuous finite elements are ideally suited for such a procedure, as the mass matrix is block diagonal. Such an implicit free-surface procedure is compatible and consistent if the three-dimensional mode is time-stepped explicitly. Unfortunately, vertical diffusion deduced from a turbulence scheme or used as a convective adjustment algorithm is often large enough for the corresponding constraint on the time step to be much more severe than the one deduced from internal gravity waves. Vertical diffusion and advection terms must often be treated implicitly.

The Finite Element Ocean Model (FEOM) uses a similar approach with an implicit vertical diffusion (Wang, 2007; Wang et al., 2008b). The momentum equation is split in two steps and an intermediate velocity is introduced to perform the implicit calculation of the elevation. Implicit vertical viscosity is neglected in the correction step, meaning that this term is computed using this intermediate velocity rather than the final corrected value. This is needed to derive the equation associated with the elevation. Such a method of substitution is similar to the Schur complement approach used by Dukowicz and Smith (1994), but the substitution is performed in the continuous space rather than at the discrete level. Working within a continuous framework, the inverse of the mass matrix $M_{\boldsymbol{u}}^{-1}$ disappears in what corresponds to the Schur complement. Therefore, the discrete operator is not the same and the two-dimensional discrete system for the elevation reads:

$$\left[M_\eta - \Delta_t L\right] X_\eta = F_\eta - \Delta_t DF_{\boldsymbol{u}},$$

where L is the discrete Laplacian matrix and Δ_t is the time step. The operator $\Delta_t L$ is used rather than $DM_{\boldsymbol{u}}^{-1}G$ and can be viewed as an approximation or an alternative choice. The same remark applies for $\Delta_t DF_{\boldsymbol{u}}$ that acts as a substitute of $DM_{\boldsymbol{u}}^{-1}F_{\boldsymbol{u}}$.

In this paper, we present an implicit mode splitting procedure used for a marine model, called SLIM (Second-generation Louvain-la-Neuve Ice-ocean Model[1]) that should be able to deal with problems ranging from local and regional scales to global scales. In a first step of the time stepper, the new elevation field is implicitly computed, and afterwards we use this value and the corresponding two-dimensional velocities in the baroclinic mode to compute the three-dimensional velocity. The

[1] `http://www.climate.be/slim`

main contribution of the time marching procedure of SLIM is that a correction term is embedded in the three-dimensional momentum equation to ensure compatibility between two- and three-dimensional velocities. Identity between depth-averaged three-dimensional velocity and two-dimensional velocity is enforced using Lagrange multipliers in the three-dimensional system It provides an implicit accurate coupling between two- and three-dimensional modes.

To illustrate the accuracy of this time discretization, we consider the simulation of Taylor caps in the wake of a tall seamount. We define the parameters of the simulation to compare the transient dynamics with results published by Chapman and Haidvogel (1992) and Ford et al. (2004). The main reason to analyze this problem is the fact that subgrid-scale parametrization is not required to generate complex baroclinic phenomena (Chapman and Haidvogel, 1992).

In a companion paper (Blaise et al., 2010), we introduced the detailed description of the space discretization. Equal-order discontinuous interpolations for the elevation and velocity fields are used. The Discontinuous Galerkin method is selected in order to accurately simulate the advection dominated processes. The model operates on prismatic meshes, obtained by extruding vertically a triangular surface grid. It relies on approximate Riemann solvers based on the wave dynamics of the system. The consistency, the accuracy and the stability of the spatial discretization were analyzed. Herein, the time integration procedure will be provided. Section 2 describes the partial differential equations considered. Section 3 defines a new time-splitting procedure with compatible discrete barotropic 2D and the baroclinic 3D problems. Implicit-Explicit (IMEX) Runge-Kutta time integrators used in the three-dimensional baroclinic marine model are explained in Section 5. A first validation of the dynamics of the model is given in Section 6. Revisiting a modified version of the flow over a tall seamount described in Blaise et al. (2010), we analyze the dynamics behavior and compare our results with previous publications. Concluding remarks are given in Section 7.

2 Governing equations

Using material parameters and notations defined in Table 1, the set of partial differential equations of the three-dimensional baroclinic free-surface model reads:

$$\frac{\partial \boldsymbol{u}}{\partial t} + \boldsymbol{\nabla}_h \cdot (\boldsymbol{u}\boldsymbol{u}) + \frac{\partial w\boldsymbol{u}}{\partial z} + f\mathbf{e}_z \wedge \boldsymbol{u} + \frac{\boldsymbol{p}}{\rho_0} + g\boldsymbol{\nabla}_h \eta = \boldsymbol{\nabla}_h \cdot (\nu_h \boldsymbol{\nabla}_h \boldsymbol{u}) + \frac{\partial}{\partial z}\left(\nu_v \frac{\partial \boldsymbol{u}}{\partial z}\right), \tag{1}$$

$$\frac{\partial \boldsymbol{p}}{\partial z} = -g\boldsymbol{\nabla}_h \rho'(T,S), \tag{2}$$

$$\boldsymbol{\nabla}_h \cdot \boldsymbol{u} + \frac{\partial w}{\partial z} = 0, \tag{3}$$

$$\frac{\partial \eta}{\partial t} + \nabla_h \cdot \int_{-h}^{\eta} \boldsymbol{u} dz = 0, \tag{4}$$

$$\frac{\partial c}{\partial t} + \boldsymbol{\nabla}_h \cdot (\boldsymbol{u}c) + \frac{\partial wc}{\partial z} = \boldsymbol{\nabla}_h \cdot (\kappa_h \boldsymbol{\nabla}_h c) + \frac{\partial}{\partial z}\left(\kappa_v \frac{\partial c}{\partial z}\right). \tag{5}$$

Coordinates and spatial operators	
x, y	Horizontal coordinates
z	Vertical coordinate, pointing upwards with its origin at the sea surface at rest
$\boldsymbol{\nabla}_h$	Horizontal gradient operator
$\boldsymbol{e}_z$	Upward unit normal
$\wedge$	Cross product symbol
Material parameters and functions	
g	Gravitational acceleration
ρ_0	Reference density
f	Coriolis parameter
h	Depth at rest
ν_h	Horizontal turbulent viscosity parameter
ν_t	Vertical turbulent viscosity parameter
κ_h	Horizontal turbulent diffusivity parameter
κ_t	Vertical turbulent diffusivity parameter
$\boldsymbol{U}$	Two-dimensional horizontal mean velocity vector
Variables	
$\boldsymbol{u}$	Horizontal three-dimensional velocity vector
w	Vertical three-dimensional velocity vector
$\boldsymbol{u}^\eta$	Surface horizontal three-dimensional velocity vector
w^η	Surface vertical three-dimensional velocity vector
$\boldsymbol{u}^{-h}$	Bottom horizontal three-dimensional velocity vector
w^{-h}	Bottom vertical three-dimensional velocity vector
η	Sea surface elevation
p	Baroclinic pressure
$\boldsymbol{p}$	Baroclinic pressure gradient
c	Three-dimensional tracer, can be S of T
S	Salinity
T	Temperature

Table 1: Notations for the three-dimensional baroclinic free-surface marine model

where the unknown fields are the horizontal velocity $\boldsymbol{u}(x, y, z, t)$, the baroclinic pressure gradient $\boldsymbol{p}(x, y, z, t) = \boldsymbol{\nabla}_h p(x, y, z, t)$, the vertical velocity $w(x, y, z, t)$, the sea surface elevation $\eta(x, y, t)$ and the tracer concentrations $c(x, y, z, t)$ that can be the temperature and/or the salinity.

Now, let us define the two-dimensional depth-averaged horizontal mean velocity:

$$\boldsymbol{U}(x, y, t) = \frac{1}{h(x, y) + \eta(x, y, t)} \int_{-h(x,y)}^{\eta(x,y,t)} \boldsymbol{u}(x, y, z, t)\ dz. \tag{6}$$

and the corresponding two-dimensional depth-averaged barotropic equations:

$$\frac{\partial \boldsymbol{U}}{\partial t} + f\mathbf{e}_z \wedge \boldsymbol{U} + g\nabla\eta = \mathbf{f}_{\mathbf{U}}, \tag{7}$$

$$\frac{\partial \eta}{\partial t} + \nabla \cdot [(h + \eta)\boldsymbol{U}] = 0, \tag{8}$$

where $\mathbf{f}_{\mathbf{U}}$ includes all the remaining terms resulting from the integration of (1). As the free-surface evolution only depends on the two-dimensional velocity $\boldsymbol{U}$, a *mode-splitting procedure* is often introduced. The two-dimensional barotropic equations

and the three-dimensional baroclinic equations are advanced in time with different schemes and/or steps. As the surface gravity waves propagate roughly two orders of magnitude faster than internal gravity waves, the three-dimensional baroclinic time step could be quite a lot larger than the two-dimensional barotropic time step. Then, it also appears attractive to use an implicit time stepper for the two-dimensional barotropic problem and an explicit time stepper for the three-dimensional baroclinic mode.

The mode-splitting procedure consists in integrating the two-dimensional barotropic equations with many time steps or an implicit scheme while the three-dimensional baroclinic equations are solved with a single step. In this procedure, the three-dimensional velocities must be calculated in such a way that their average matches the velocities of the barotropic mode to obtain compatibility. Two critical conditions must be fulfilled:

- The two-dimensional $\boldsymbol{U}$ and three-dimensional $\boldsymbol{u}$ discrete representations of the velocities must be compatible. In other words, using the discrete version of equation (4) or (8) must produce exactly the same result. It means that $\boldsymbol{U}$ must be recovered by performing at a discrete level the depth-average of $\boldsymbol{u}$. The basic idea is that the equivalence properties that exist in the continuous realm must be preserved in the discrete realm. It is the so-called *compatibility condition*.
- The discrete numerical mode must be consistent by being able to advect a constant concentration of a given tracer exactly, up to machine accuracy. To achieve this, the advection term of the tracer equation must degenerate to the continuity equation when a constant tracer concentration is considered (White et al., 2008). As the compatibility of $\boldsymbol{u}$ and $\boldsymbol{U}$ is needed to obtain the compatibility of w and η, ensuring impermeability at the sea surface, the compatibility can be viewed as a mandatory requirement to ensure this *consistency condition*. Obviously, this is not the usual consistency meaning that the discrete formulation converges to the continuous equation as the mesh size goes for zero.

3 Compatible discrete barotropic and baroclinic problems

In the current SLIM model, we use an implicit mode splitting procedure. Firstly, the elevation and two-dimensional velocities are implicitly computed: it is the two-dimensional barotropic problem. Then, we use this elevation and those two-dimensional velocities to obtain the three-dimensional velocities: it is the three-dimensional baroclinic problem.

The major novelty of the implemented approach of the SLIM model is that the correction term is embedded in the three-dimensional momentum equation to ensure compatibility between two-dimensional and three-dimensional velocities. Equality between depth-averaged three-dimensional velocity and two-dimensional velocity is enforced using Lagrange multipliers in the three-dimensional baroclinic problem. The implicit terms in the momentum equation are computed using a three-dimensional velocity in agreement with the two-dimensional mode. This ensures for instance that, if the Coriolis term is treated semi-implicitly, it influences the dynamics of both modes in the same way.

In order to describe the whole procedure, let us first define the baroclinic and the barotropic problems.

– The two-dimensional barotropic problem consists in finding $(\boldsymbol{U}, \eta)$ such that:

$$\frac{\partial \boldsymbol{U}}{\partial t} + f\mathbf{e}_z \wedge \boldsymbol{U} + g\nabla\eta = \mathbf{f}_{\mathbf{U}}, \tag{9}$$

$$\frac{\partial \eta}{\partial t} + \nabla \cdot [(h+\eta)\boldsymbol{U}] = 0, \tag{10}$$

– The three-dimensional baroclinic problem consists in finding $(\boldsymbol{u}, \boldsymbol{\lambda})$ such that:

$$\frac{\partial \boldsymbol{u}}{\partial t} + f\mathbf{e}_z \wedge \boldsymbol{u} + \frac{\partial w\boldsymbol{u}}{\partial z} - \frac{\partial}{\partial z}\left(\nu_v \frac{\partial \boldsymbol{u}}{\partial z}\right) + \boldsymbol{\lambda}, = \mathbf{f}_{\mathbf{u}}, \tag{11}$$

$$\int_{-h}^{\eta} \boldsymbol{u}\, dz = \boldsymbol{U}, \tag{12}$$

where all terms explicitly time-integrated are included in the right-hand side $\mathbf{f}_{\mathbf{U}}$ and $\mathbf{f}_{\mathbf{u}}$ respectively. In the three-dimensional momentum equation, we add a volume force $\boldsymbol{\lambda}$. This force will act to ensure compatibility between both velocity representations. Equations (11)-(12) are the usual Euler-Lagrange equations of the saddle-point problem.

Now, we introduce the finite element mesh and the discrete discontinuous approximations of the field variables of the model (η, $\boldsymbol{u}$, $\boldsymbol{U}$, $\boldsymbol{\lambda}$) involved in the barotropic and the baroclinic modes. The three-dimensional mesh is made up of prismatic elements, as illustrated in Figure 1, and is obtained from the extrusion of triangular two-dimensional elements. The vertical length scale is typically much smaller than the horizontal length scale. In other words, the prisms are thin. We choose prismatic elements to obtain a mesh unstructured in the horizontal direction, and structured in the vertical direction. The two-dimensional fields η, $\boldsymbol{U}$ and $\boldsymbol{\lambda}$ are discretized with P_1^{DG} elements onto the two-dimensional mesh of triangles. The three-dimensional fields ($\boldsymbol{u}$) are discretized on the mesh of prisms and the corresponding shape functions are obtained as the tensorial product of the linear discontinuous triangle P_1^{DG} an the linear one-dimensional element L_1^{DG}.

In the space discretization of the SLIM model (Blaise et al., 2010), the discrete free-surface equation is obtained as the aggregation of the discrete horizontal divergence of the three-dimensional horizontal velocity with a bottom boundary term. A similar approach can be done for the barotropic and baroclinic momentum equations. We aggregate the three-dimensional horizontal momentum equation (11), without the Lagrange multipliers $\boldsymbol{\lambda}$. This will lead to equation (9), which corresponds to the non-conservative form of the momentum equation of the shallow water equations. To exactly obtain this equation (9), the test function of the three-dimensional momentum equation is divided by the depth.

Then we add to the linear system corresponding to the horizontal three-dimensional momentum equation for the degrees of freedom of a column of prisms, six lines and columns corresponding to two Lagrange multipliers for each of the three surface nodes (considering linear shape functions). The lines correspond to the compatibility constraint:

$$\sum_{e=1}^{N_e} < \widehat{\lambda} \cdot (\boldsymbol{u} - \boldsymbol{U}) >_e = 0, \tag{13}$$

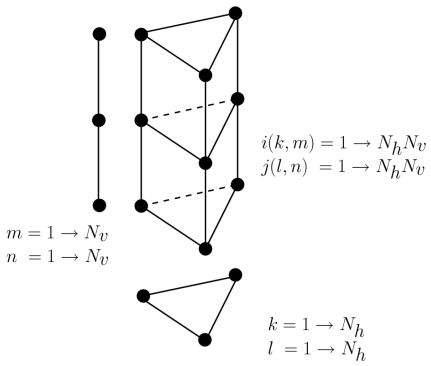

Field		Finite element space
Free surface elevation	η	P_1^{DG}
Lagrange multiplier	λ	P_1^{DG}
Horizontal two-dimensional velocity vector	$\boldsymbol{U}$	P_1^{DG}
Horizontal three-dimensional velocity vector	$\boldsymbol{u}$	$P_1^{DG} \times L_1^{DG}$

Fig. 1: Summary of the finite element spaces used for each field. Triangular linear elements are noted P_1 while vertical linear elements are noted L_1. Indices indicated on the mesh correspond to the nodal discrete values. The global indices $i(k,m)$ and $j(k,m)$ are a function of the horizontal position and the vertical position.

while the columns correspond to the fictitious force:

$$\sum_{e=1}^{N_e} \left[< \widehat{\boldsymbol{u}} \cdot \frac{\partial \boldsymbol{u}}{\partial t} >_e + \cdots + < \widehat{\boldsymbol{u}} \cdot \boldsymbol{\lambda} >_e \right] = 0, \tag{14}$$

with λ the Lagrange multiplier field, and $\hat{\boldsymbol{\lambda}}$ the corresponding test functions. The baroclinic mode is compatible with the barotropic mode, and mass conservation is ensured. The inconsistency is only due to the commutation between spatial discretization and depth integration needed to make the vertical dynamics terms disappear in the two-dimensional momentum equation.

Both discrete barotropic and baroclinic problems can be then written with matrix notations.

– The two-dimensional discrete barotropic problem reads:

$$\begin{bmatrix} M_{\boldsymbol{U}} & G \\ D & M_\eta \end{bmatrix} \begin{bmatrix} X_{\boldsymbol{U}} \\ X_\eta \end{bmatrix} = \begin{bmatrix} F_{\boldsymbol{U}} \\ 0 \end{bmatrix}, \tag{15}$$

– The three-dimensional discrete baroclinic problem reads:

$$\begin{bmatrix} M_{\boldsymbol{u}} & E^T \\ E & 0 \end{bmatrix} \begin{bmatrix} X_{\boldsymbol{u}} \\ X_\lambda \end{bmatrix} = \begin{bmatrix} F_{\boldsymbol{u}} \\ F_\lambda \end{bmatrix}, \tag{16}$$

where E is the matrix associated with the discrete compatibility constraint. The effect of these Lagrange multipliers is to correct the discrepancy due to the different treatment of vertical terms in the baroclinic and barotropic modes.

4 Global time-stepping algorithm

The global time-stepping algorithm be summarized as follows.

1. Evaluate the terms common for both 2D and 3D problems
2. Solve the 2D barotropic problem to obtain $\boldsymbol{U}$ and η
3. For each column of prisms, solve the 3D baroclinic problem
   (a) Evaluate the implicit terms for the momentum equation
   (b) Evaluate the terms for the compatibility constraint
   (c) Solve the local linear system to obtain $\boldsymbol{u}$ and λ
4. Integrate the continuity equation to obtain w
5. For each column of prisms, solve the tracer equations
   (a) Evaluate the implicit terms
   (b) Solve the local linear system to obtain T and/or S
6. Calculate the density ρ
7. Integrate the baroclinic pressure gradient $\boldsymbol{p}$

We build the global matrix for the two-dimensional barotropic mode, and solve the corresponding linear system with a GMRES iterative solver preconditioned with a block factorization combined with an additive-Schwartz coupling. An efficient implementation will avoid to duplicate computations for the two-dimensional barotropic mode and the three-dimensional baroclinic mode and will therefore compute all common term in a preliminary step.

For the three-dimensional momentum equations, the terms related to surface gravity waves, vertical advection, vertical diffusion, and Coriolis are treated (semi-)implicitly, while horizontal advection and diffusion are explicit. However, the Coriolis term could be stepped with about 1 h explicitly, and the necessity to treat vertical advection implicitly or explicitly depends on applications (coastal or global) and resolution as well. Moreover, horizontal advection is not always a much slower phenomenon compared with vertical advection. Therefore, this selection strongly depends on the application. We do not assemble the linear system for the three-dimensional momentum equation, because the mass matrix for the Discontinuous Galerkin methods is block-diagonal per element and all implicit terms are local on vertically aligned prisms. Therefore, the linear system is block-diagonal for each column of

prisms. Each block is then solved locally using a sparse direct solver. The memory usage is not larger than for an explicit method, and this solution strategy is intrinsically scalable. As time-integration scheme, we use implicit-explicit (IMEX) methods. Such an approach allow us to treat implicitly the linear terms corresponding to the stiff part of the problem, while treating explicitly the other terms.

The continuity equation is then locally solved, because only stacked prisms are coupled together. Further, the information only goes from bottom to top, as we treat this equation as a steady advection equation, so that block per element Gauss-Seidel sweeping from bottom to top gives the exact result in a single iteration. Tthe matrix for a column of prisms is block triangular. The equation for the pressure gradient force can also be solved for each column of prisms independently.

5 Implicit-explicit Runge-Kutta methods

In IMEX methods (Ascher et al., 1995, 1997), only the most critical terms are integrated implicitly. In our three-dimensional baroclinic free-surface model, we use Runge-Kutta IMEX methods. Those methods are self-starting. Moreover, the combination of Discontinuous Galerkin methods with Runge-Kutta methods is known to be efficient (Cockburn and Shu, 2001).

The spatial discretization of the three-dimensional baroclinic problem and the two-dimensional barotropic problem leads to systems of ordinary differential equations of the form:

$$\boldsymbol{y}'(t) = \boldsymbol{f}(\boldsymbol{y}(t), t), \tag{17}$$

where $\boldsymbol{y}(t)$ denotes the vector of all discrete degrees of freedom of a step (barotropic, baroclinic or tracer problems) of the time marching algorithm. To integrate such an ordinary differential equation, explicit Runge-Kutta methods are quite popular. As a typical example, the second order explicit method of Heun consists of calculating $\boldsymbol{y}_{n+1} \approx \boldsymbol{y}(t_{n+1})$ from $\boldsymbol{y}_n = \boldsymbol{y}(t_n)$ with the following sequence:

$$\begin{cases} \boldsymbol{K}_1 = \boldsymbol{f}(\boldsymbol{y}_n, t_n), \\ \boldsymbol{K}_2 = \boldsymbol{f}(\boldsymbol{y}_n + \Delta_t \boldsymbol{K}_1, t_n + \Delta_t), \\ \boldsymbol{y}_{n+1} = \boldsymbol{y}_n + \Delta_t \left(\boldsymbol{K}_1 + \boldsymbol{K}_2\right)/2, \end{cases} \tag{18}$$

where Δ_t is the time interval. The accuracy of the discrete time integration performed with the Heun scheme is $\mathcal{O}(\Delta_t^2)$. Typically, the accuracy is often directly related to the number of stages (the number of $\boldsymbol{K}_i$ to be computed). In a more general way, a explicit or implicit Runge-Kutta method with k stages is defined by the following procedure:

$$\begin{cases} \boldsymbol{K}_i = \boldsymbol{f}\left(\boldsymbol{y}_n + \sum_{j=1}^{k} a_{ij} \Delta_t \boldsymbol{K}_j, t_n + c_i \Delta_t\right), \qquad i = 1 \dots k, \\ \boldsymbol{y}_{n+1} = \boldsymbol{y}_n + \Delta_t \left(\sum_{j=1}^{k} b_j \boldsymbol{K}_j\right). \end{cases} \tag{19}$$

A very convenient and compact way to define a Runge-Kutta method consists in having recourse to the three arrays a_{ij}, b_j, and c_i, usually represented as the so-called *Butcher tableau* defined by:

$$\left[\begin{array}{c|c} c_i & a_{ij} \\ \hline & b_j \end{array}\right] \tag{20}$$

In explicit Runge-Kutta schemes, the non-vanishing entries of the array a are only located in the left lower triangular part of the matrix with zeros on the diagonal and the right upper triangular part. As an example, the Butcher tableau of the Heun explicit method (18) is given by:

$$\left[\begin{array}{c|c} c_i & a_{ij} \\ \hline & b_j \end{array}\right] = \left[\begin{array}{c|cc} 0 & 0 & 0 \\ 1 & 1 & 0 \\ \hline & \frac{1}{2} & \frac{1}{2} \end{array}\right]$$

In implicit Runge-Kutta methods, the upper triangular of the array a contains non-zero entries. In these implicit schemes, it is possible to consider two classes: implicit Runge-Kutta methods (IRK) and diagonally implicit Runge-Kutta (DIRK). For IRK schemes, the array a is full and it is required to solve all the stages at the same time. Obviously, it can be extremely expensive and it is not very popular. In general, Diagonal Implicit Runge-Kutta (DIRK) schemes are usually resorted to, where the upper right triangular part of the array a is empty. In this case, each stage can be solved in an independent way. Moreover, Single Diagonally Implicit Runge-Kutta (SDIRK) are often used when the diagonal coefficients are equal. Accordingly for a linear problem, the matrix of the corresponding linear system will be the same for all stages.

Implicit-Explicit Runge Kutta (IMEX) schemes simply requires the splitting of the function $\boldsymbol{f}$ into a part to be integrated explicitly and a part that will be handled by an implicit scheme. We decompose the ordinary differential equation (17) in the following way:

$$\boldsymbol{y}'(t) = \overbrace{\boldsymbol{f}^{\text{expl}}(\boldsymbol{y}(t),t) + \boldsymbol{f}^{\text{impl}}(\boldsymbol{y}(t),t)}^{\boldsymbol{f}(\boldsymbol{y}(t),t)}, \tag{21}$$

where $\boldsymbol{f}^{\text{expl}}$ and $\boldsymbol{f}^{\text{impl}}$ represent the terms treated explicitly and implicitly, respectively. The explicit terms of the three-dimensional baroclinic mode are typically the nonlinear advection and the horizontal diffusion terms, while the terms corresponding to the gravity waves, the Coriolis force and the vertical diffusion are solved with the (semi-)implicit method.

The IMEX method of order k consists in using a SDIRK method with $k-1$ stages combined with an explicit RK scheme with k stages. This time stepper scheme is

defined by:

$$\boldsymbol{K}_1^{\text{expl}} = \boldsymbol{f}^{\text{expl}}(\boldsymbol{y}_n, t_n)$$

For $i = 2 \dots k$

$$\begin{cases} \boldsymbol{K}_i^{\text{impl}} = \boldsymbol{f}^{\text{impl}}(\underbrace{\boldsymbol{y}_n + \Delta_t \left(\sum_{j=1}^{i} a_{ij}^{\text{impl}} \boldsymbol{K}_j^{\text{impl}} + \sum_{j=1}^{i-1} a_{ij}^{\text{expl}} \boldsymbol{K}_j^{\text{expl}} \right)}_{\widehat{\boldsymbol{y}}_i}, t_n + c_i \Delta_t), \\ \boldsymbol{K}_i^{\text{expl}} = \boldsymbol{f}^{\text{expl}}(\widehat{\boldsymbol{y}}_i, t_n + c_i \Delta_t), \end{cases}$$

$$\boldsymbol{y}_{n+1} = \boldsymbol{y}_n + \Delta_t \left(\sum_{j=1}^{k} b_j^{\text{impl}} \boldsymbol{K}_j^{\text{impl}} + b_j^{\text{expl}} \boldsymbol{K}_j^{\text{expl}} \right). \tag{22}$$

IMEX schemes can also be defined with two Butcher tableau corresponding to the implicit and the explicit part respectively. In order to synchronize the stages, a unique c array applies to both methods and an initial empty stage is added to the implicit scheme and the corresponding arrays are padded with zeros.

To obtain a suitable discretization for linear finite elements, it seems logical to have the same accuracy in time and space and to consider a second order scheme in time. Spatial and temporal discretization errors will then converge at the same rate when the mesh is refined, the time step being adapted in accordance with the CFL condition. The implicit explicit Runge-Kutta methods used in the three-dimensional baroclinic model were derived in Ascher et al. (1997) and his Butcher tableaux read:

$$\left[\begin{array}{c|c} c_i & a_{ij}^{\text{impl}} \\ \hline & b_j^{\text{impl}} \end{array}\right] = \left[\begin{array}{c|cccc} 0 & 0 & 0 & 0 \\ \gamma & 0 & \gamma & 0 \\ 1 & 0 & 1-\gamma & \gamma \\ \hline & 0 & 1-\gamma & \gamma \end{array}\right], \tag{23}$$

$$\left[\begin{array}{c|c} c_i & a_{ij}^{\text{expl}} \\ \hline & b_j^{\text{expl}} \end{array}\right] = \left[\begin{array}{c|cccc} 0 & 0 & 0 & 0 \\ \gamma & \gamma & 0 & 0 \\ 1 & \delta & 1-\delta & 0 \\ \hline & \delta & 1-\delta & 0 \end{array}\right], \tag{24}$$

with $\gamma = (2 - \sqrt{2})/2$ and $\delta = 1 - 1/(2\gamma)$. The IMEX method consists in using a SDIRK method with 2 stages combined with an explicit RK scheme with 3 stages. Some simplifications in the calculation can be deduced from those Butcher tableau. As the last line of the matrix a exactly corresponds to the line b, the final update can be obtained directly from the last estimate $\widehat{\boldsymbol{y}}_3$ obtained for the vector $\boldsymbol{y}$. Finally the last entry of b^{expl} is zero and the last explicit stage is not needed. In short, we only need to calculate two times the explicit part $\boldsymbol{f}^{\text{expl}}$ and to solve two times the implicit system associated with $\boldsymbol{f}^{\text{impl}}$. This system has the same matrix but a different right-hand side. In a systematic way, the IMEX procedure for the three-dimensional baroclinic model can be cast in the following sequence:

1. Calculate $\boldsymbol{K}_1^{\text{expl}} = \boldsymbol{f}^{\text{expl}}(\boldsymbol{y}_n, t_n)$

2. Obtain $\boldsymbol{K}_2^{\text{impl}}$ and $\widehat{\boldsymbol{y}}_2$ by solving:

$$\boldsymbol{K}_2^{\text{impl}} = \boldsymbol{f}^{\text{impl}}(\underbrace{\boldsymbol{y}_n + \Delta_t(\gamma \boldsymbol{K}_1^{\text{expl}} + \gamma \boldsymbol{K}_2^{\text{impl}})}_{\widehat{\boldsymbol{y}}_2}, t_n + \Delta_t \gamma)$$

3. Calculate $\boldsymbol{K}_2^{\text{expl}} = \boldsymbol{f}^{\text{expl}}(\widehat{\boldsymbol{y}}_2, t_n + \Delta_t \gamma)$

4. Obtain $\boldsymbol{K}_3^{\text{impl}}$ and $\widehat{\boldsymbol{y}}_3$ by solving:

$$\boldsymbol{K}_3^{\text{impl}} = \boldsymbol{f}^{\text{impl}}(\underbrace{\boldsymbol{y}_n + \Delta_t(\delta \boldsymbol{K}_1^{\text{expl}} + (1-\delta)\boldsymbol{K}_2^{\text{expl}} + (1-\gamma)\boldsymbol{K}_2^{\text{impl}} + \gamma \boldsymbol{K}_3^{\text{impl}})}_{\widehat{\boldsymbol{y}}_3}, t_n + \Delta_t)$$

5. Set $\boldsymbol{y}_{n+1} = \widehat{\boldsymbol{y}}_3$

6 Numerical results

Internal waves in the lee of a moderately tall seamount were simulated in Blaise et al. (2010). In this paper, we consider a similar set-up to compare the transient dynamics with results published by Chapman and Haidvogel (1992) and in Section 3c of Ford et al. (2004). This set-up is selected because there is no need for subgrid-scale parametrization to create complex baroclinic phenomena. The flow is stratified, but subcritical: there is no internal wave break-up. No boundary layer appears, as a slip condition at the seabed is prescribed. In the first part of this work (Blaise et al., 2010), the height of the seamount was 30% of the total depth, and a complicated internal wave structure developed in the wake of the seamount. Now, we consider that the height of the seamount is 90% of the total depth in order to observe some recirculation patterns in the wake of the seamount.

The first computation of a three-dimensional linearly stratified flow over a Gaussian seamount was done by Huppert and Bryan (1976) with the model of Bryan (1969). A detailed numerical study of flows past Gaussian seamounts can be found in Chapman and Haidvogel (1992, 1993). The strengths and weaknesses of a few other models have been assessed by simulating flow past seamounts: MITgcm (Adcroft et al., 1997), ICOM (Ford et al., 2004) and FEOM (Wang et al., 2008b). Our numerical simulations will be performed in order to draw some comparisons with previous computations.

The computational domain is an aquaplanet, as it allows us to avoid open boundary conditions. Figure 2 shows a close-up view of the mesh and the bathymetry near the seamount. The mesh resolution is refined in the lee of the seamount, to allow for an accurate representation of the shedded vortex described in Chapman and Haidvogel (1992) and Ford et al. (2004). The edge-length in the most refined zone is 2 km. This mesh is made up of 13836 triangles extruded into 20 σ layers.

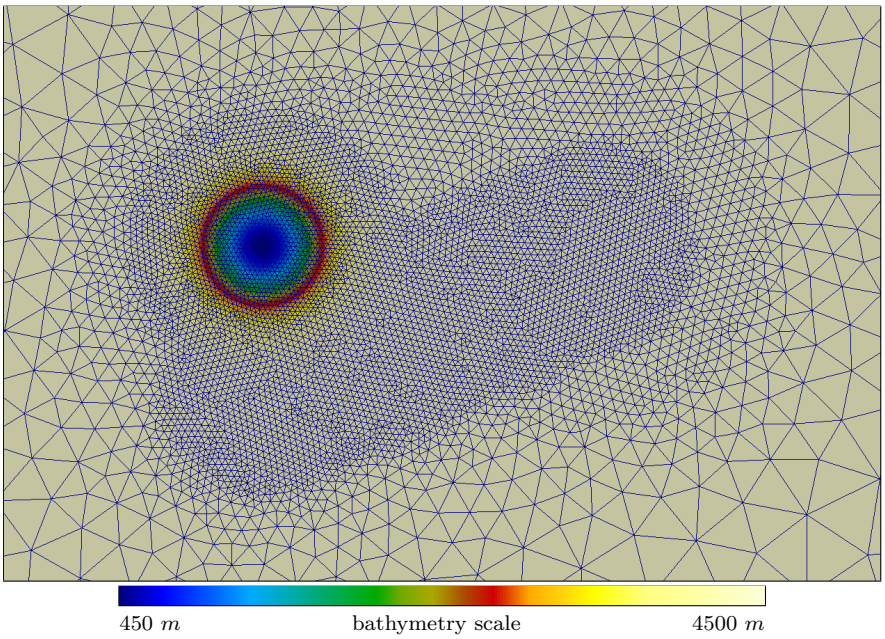

Fig. 2: Close-up view on the mesh and the bathymetry around the seamount. The mesh is refined in the lee of the seamount.

The geometry of the problem is defined by a Gaussian seamount located at a latitude of 45^o degrees North. The bathymetry reads:

$$1 - \frac{h(x,y)}{H} = \delta \exp\left(\frac{\left(x - \frac{R}{2}\right)^2 + \left(y - \frac{R}{2}\right)^2 + \left(z - \frac{R}{\sqrt{2}}\right)^2}{-L^2} \right), \tag{25}$$

where $H = 4.5\ km$ is the total depth, $\delta = 0.9$ is the relative height of the seamount, $R = 6\ 372\ \ km$ is Earth radius and $L = 25\ km$ is the length scale of the seamount. The coordinates x, y and z are relative to the global Cartesian reference coordinates axis located in the center of the sphere. The flow simulation is initiated with a global zonal geostrophic equilibrium ignoring the seamount. In other words, the initial guess of the calculation is the same as in the Testcase 5 of Williamson et al. (1992) where the velocity field only exhibits a non vanishing East component u_e. In this testcase, the elevation and velocity fields are respectively given by

$$\frac{\eta}{U^2/g} = -\frac{z^2}{R^2}\left(1 + \sqrt{2}\,\frac{R\Omega}{U}\right), \tag{26}$$

$$\frac{u_e}{U} = \sqrt{\frac{x^2 + y^2}{R^2}}, \tag{27}$$

where $U = 0.258\ m\ s^{-1}$ is the velocity scale at a latitude of 45^o degree North, $\Omega = 7.292 \times 10^{-5}\ s^{-1}$ is Earth rotation rate, and $g = 9.81\ ms^{-2}$ is the gravitational

acceleration. We only consider the density deviation ρ' as the unique tracer of the model and the initial value of the density deviation is a linear function of the vertical coordinate, with vanishing mean. The derivative of the density with respect to the vertical coordinate is given by $\partial\rho/\partial z = -3.43 \times 10^{-5}\ kg\ m^{-4}$ and the reference density is selected as $\rho_0 = 1025\ kg\ m^{-3}$. The turbulent viscosities and diffusivities are given by: $\nu_h = \kappa_h = 6.45\ m^2\ s^{-1}$, $\nu_v = 0.0001\ m^2\ s^{-1}$ and $\kappa_v = 0$. With those parameters, we consider that the flow is characterized by the same four dimensionless numbers as that in Section 3.c of Ford et al. (2004). These dimensionless number are defined as follows:

- Seamount ratio $\qquad \delta = 0.9$

- Rossby number $\qquad Ro = \dfrac{U}{fL} = 0.1$

- Reynolds number $\qquad Re = \dfrac{UL}{\nu_h} = 1000$

- Burger number $\qquad Bu = \dfrac{NH}{fL} = \sqrt{\dfrac{-g}{\rho_0}\dfrac{\partial\rho}{\partial z}}\dfrac{H}{fL} = 1$

where N is the Brunt-Väisälä frequency.

The critical numerical parameter in the three-dimensional baroclinic model is the jump penalty coefficient γ of the Lax-Friedrichs solver. For this problem, we select $\gamma = 6\ m\ s^{-1}$. Here, we select a slightly higher γ than for the simulations presented in Blaise et al. (2010), because the height of the seamount is quite larger. Above the seamount, the density profile may be significantly altered and this parameter must be an upper bound of the phase speed of the fastest wave. For discontinuous linear elements combined with the second order explicit Runge-Kutta time stepper (Chevaugeon et al., 2007) used in this simulation, the relevant CFL conditions reads:

$$\Delta_t < \frac{\Delta_x}{3\gamma} \tag{28}$$

The smallest edge length is 2 km and the relevant length is the inradius of this smallest triangle. Therefore, $\Delta_x = 0.29 \times 2\ km$ and the greatest time step to avoid instabilities is 32 s. In this simulation, we use a time step of 20 s.

The two-dimensional dynamics of flows past isolated obstacles is already complicated. Verron and Le Provost (1985) give a detailed analysis of the flows that occurs over an isolated seamount, using a two-dimensional model of the quasi-geostrophic equations. A clockwise vortex is always trapped over the seamount, but several transient regimes can occur. For strong flows, such as the configuration given in Blaise et al. (2010), the counter-clockwise vortex generated in the initiation flow phase is directly advected downstream. For weak flows, such as the current configuration, a stronger interaction between the two eddies occurs and the counter-clockwise vortex is shifted to the right and trapped in the vicinity of the seamount, leading to a double vortex structure.

Two-dimensional daily depth-averaged velocities and the sea surface deviation are shown in Figure 3. The sea surface deviation is defined as the difference between the

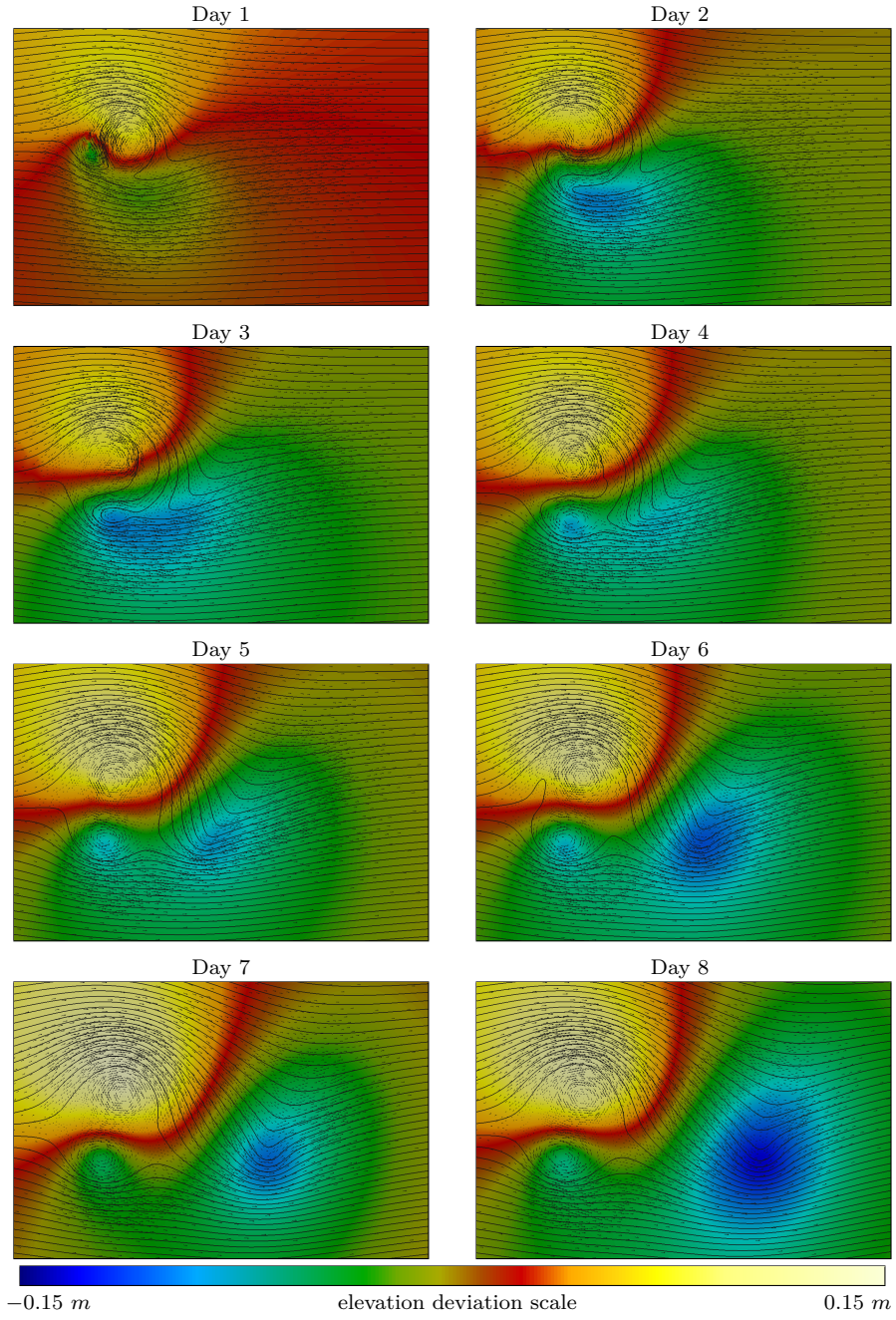

Fig. 3: Two-dimensional flow ($\delta = 0.9$). Colors denotes sea surface deviation with respect to initial geostrophic equilibrium. Glyphs represents two-dimensional mean velocities. The black continuous lines are the instantaneous streamlines.

sea-surface elevation and initial elevation corresponding to the geostrophic elevation. As the flow is impulsively started, the free-surface is raised in front of the seamount, and lowered behind it. Geostrophic adjustment induces two counter-rotating eddies, the one in front of the seamount being clockwise. Under a rigid-lid approximation, this adjustment can be interpreted in terms of vortex compression and stretching (Verron and Le Provost, 1985). These two vortices progress clockwise around the seamount, with a time scale much smaller than the advective one. In Figure 3, we see that at day one, the two vortices have already rotated almost half a turn clockwise. The rotation of this vortex pair can be explained in terms of topographic Rossby waves. Depth variation induces effects similar to Coriolis parameter variation, i.e. the β effect. These waves propagate with the shallowest area on their right (Cushman-Roisin, 1994, Section 6.5). This leads to a clockwise progression of the vortex pair. The phase speed aligned with isobaths is proportional to the bottomslope. For a Gaussian shaped bathymetry, the maximum speed will therefore occur at a radius corresponding to the inflexion point of the Gaussian, which in this case is $L/\sqrt{2}$. The initially circularly shaped vortices tend to become spiral shaped, as explained in Johnson (1984). The flow still exhibit some global coherent structures and have been modeled with two-dimensional approximations such as quasi-geostrophic equations (Johnson, 1984; Verron and Le Provost, 1985).

The vertical structure of the flow can be observed from the isosurfaces of the density perturbation given in Figure 4. The density perturbation is defined as the difference between density deviation field ρ' and the initial density deviation. As the flow is quasi-geostrophic, the density perturbation is an image of the vorticity, as the elevation deviation. In fact, a complex interaction takes place, where the counter-clockwise vortex undergoes a stretching and breaking sequence that generates internal waves in the lee of the seamount. This can be observed in Figure 5 where a horizontal slice in the density perturbation at a depth of 400 m is displayed.

Using the quasi-geostrophic equations, Johnson (1984) shows that the starting flow over a smooth obstacle leads to topographic Rossby waves that rotate clockwise around the obstacle. For a parabolic obstacle, spiral waves are observed. These internal topographic Rossby waves are progressing as spirals between days 2 and 3. These waves can be clearly detected from the density perturbation isovalues at a depth of 4000 m in Figure 6. The counter-clockwise vortex then breaks into two well separated parts. The first one is trapped on the right side of the seamount (looking downstream), while the second one is ejected and transported at the mean speed of the flow. Indeed, two recirculation cells exist. One is trapped over the seamount, and the other one is located on the right side of the seamount.

Finally, it is instructive to perform some comparisons between our numerical simulations and some previous calculations. A quite similar flow in a rectangular domain with constant Coriolis parameter was simulated by several authors:

- Chapman and Haidvogel (1992) use a rigid lid model with finite-difference horizontal discretization and spectral vertical discretization, and along sigma levels hyperviscous dissipation.
- Adcroft et al. (1997) use a rigid lid finite-volume model, but only provide results after 10 days.
- Ford et al. (2004) use a finite-element non-hydrostatic model, with rigid-lid approximation and Laplacian dissipation.

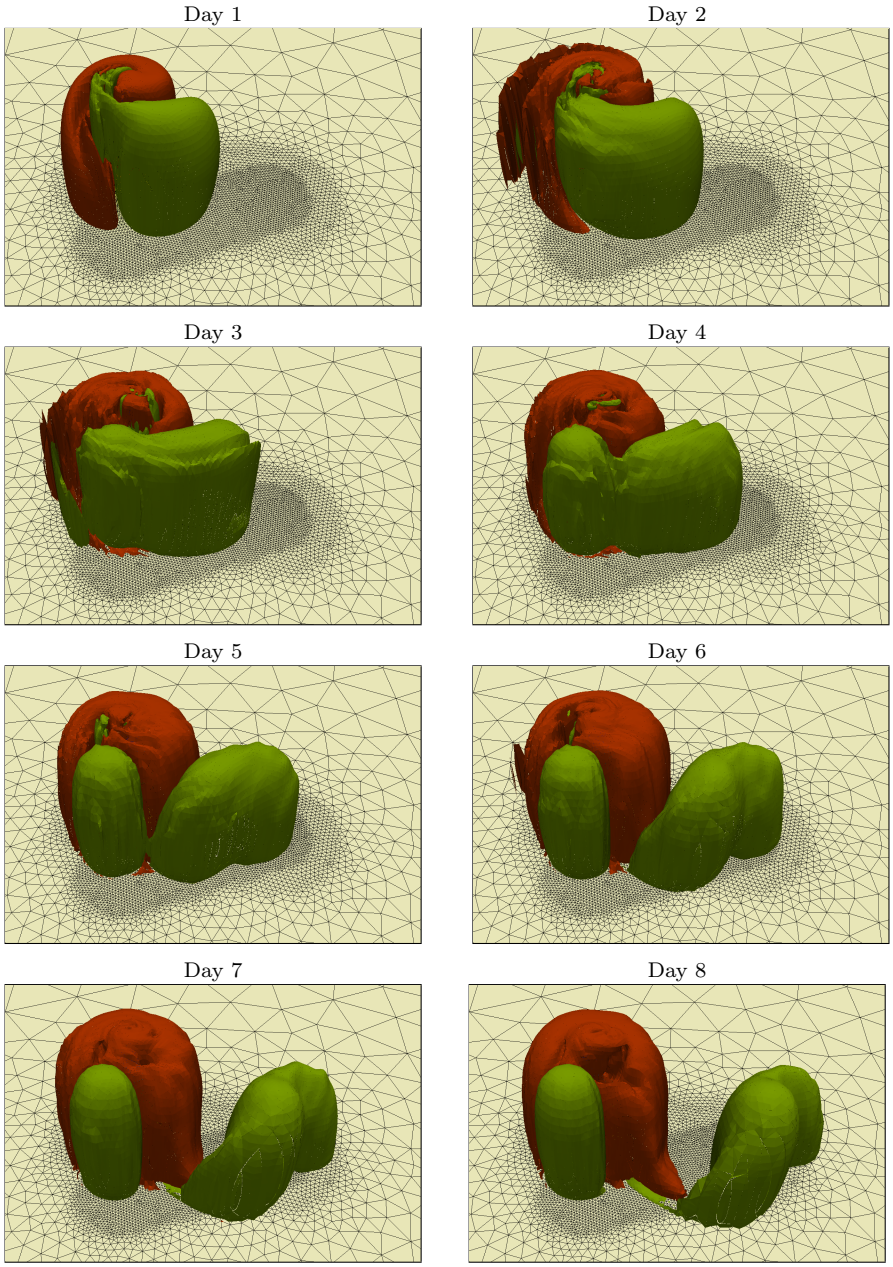

Fig. 4: Time evolution of the isosurfaces of the density perturbation. Isovalues of density perturbation of $-0.001kg\ m^{-3}$ are in green. Isovalues of density perturbation of $0.001kgm^{-3}$ are in red. The two-dimensional mesh is given on the sea bottom.

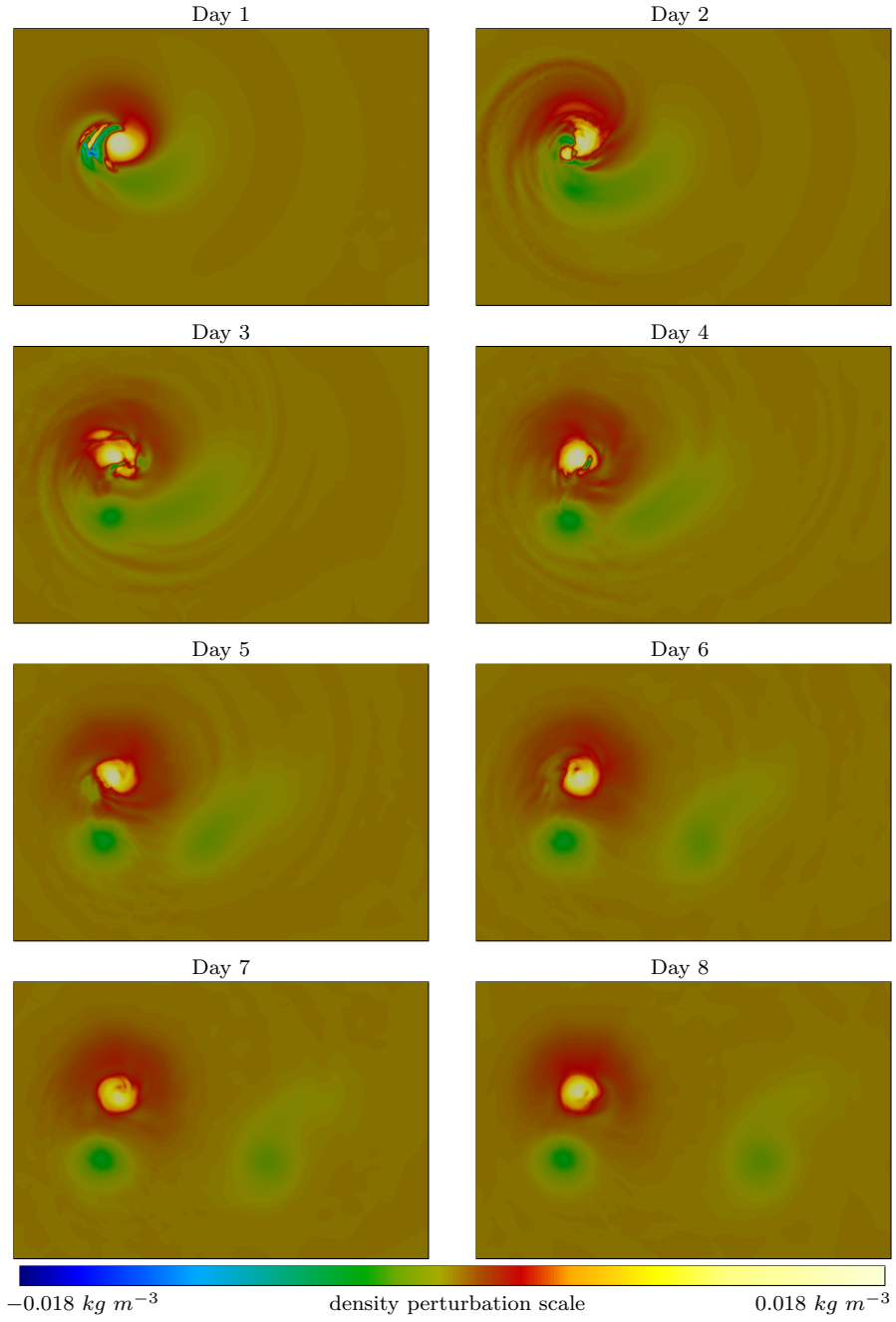

Fig. 5: Density perturbation for a horizontal cut at 400 m depth.

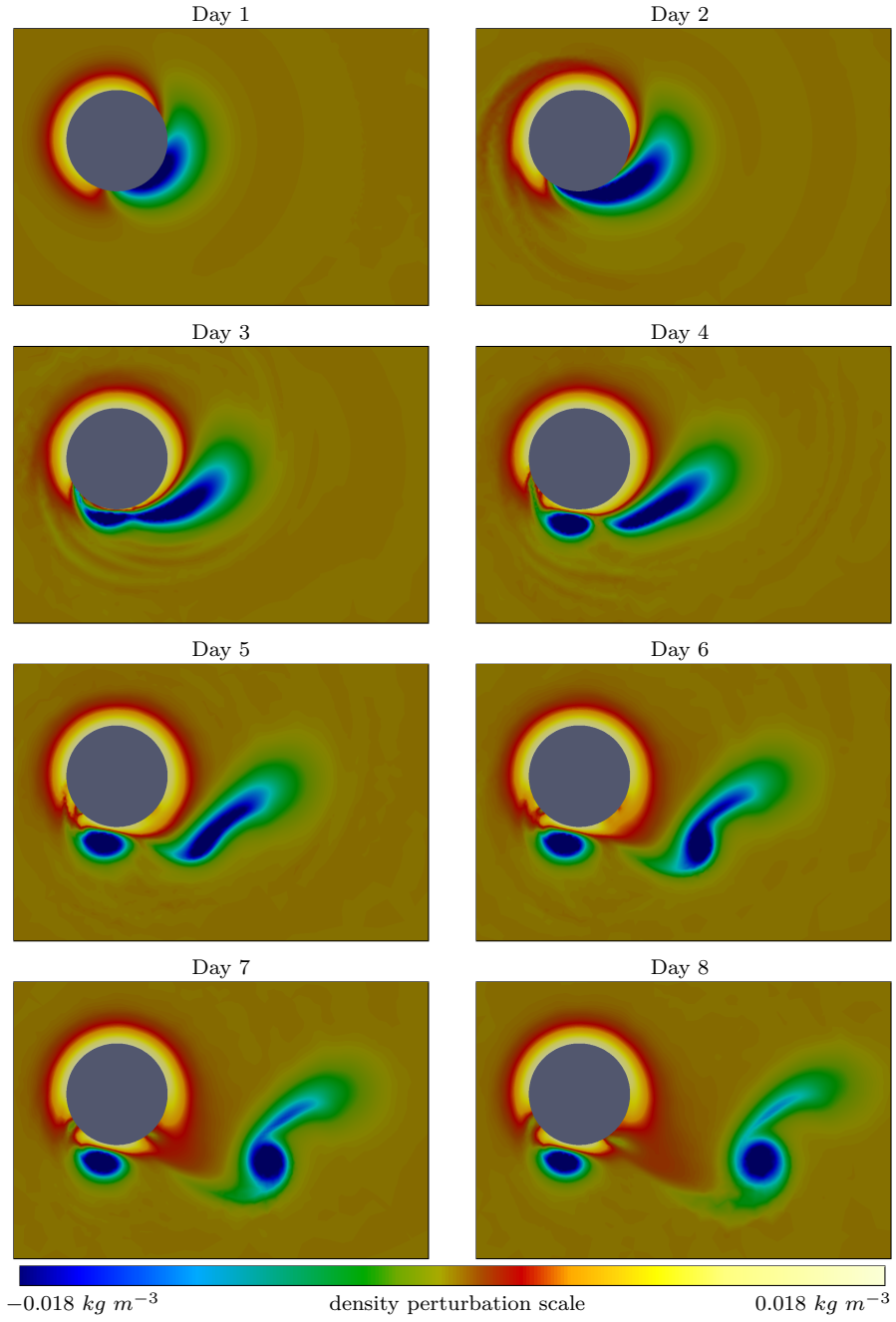

Fig. 6: Density perturbation for a horizontal cut at 4000 m depth.

The problem is not exactly the same as we introduce the full Coriolis term on the sphere, while the f-plane approximation is considered in those previous calculations. However, this should not induce significant flow discrepancy, as we focus on the small scale, where the variations of the Coriolis parameter are negligible compared to other effects, such as the influence of the bathymetry.

For the early stages of the flow, our model exhibits numerous wave phenomena. In Figures 7 and 8, we show a detailed comparison with the results obtained by Chapman and Haidvogel (1992). Both simulations produce a quite similar behavior during the first two days. However, our calculation exhibits significant internal spiral waves that do not appear in Chapman and Haidvogel (1992) and Ford et al. (2004). This observation could be explained by the rather smaller dissipation introduced by our numerical scheme. Those waves could also be due to an interaction with the free-surface, while Chapman and Haidvogel (1992) and Ford et al. (2004) use the rigid lid approximation. In Figure 9, we observe that the counterclockwise eddy is stretched and breaks up, one part being trapped near the seamount while the other is shedded. In our computation, the break up of the eddy happens much faster. The trapped eddy is much larger, and the shedded eddy tends to become much more circular. This difference can be explained easily: Ford et al. (2004) and Chapman and Haidvogel (1992) carry out their computation in a box domain, with lateral walls. Indeed, these walls are too close to the seamount for their influence to be negligible. Figure 10 sketches the elevation deviation after 3 and 7 days, along with black lines located where the lateral walls are found in Ford et al. (2004). It can be seen that the flow clearly varies along those boundaries. When those boundaries are present, the counterclockwise vortex cannot develop laterally, and this prevents its breakup.

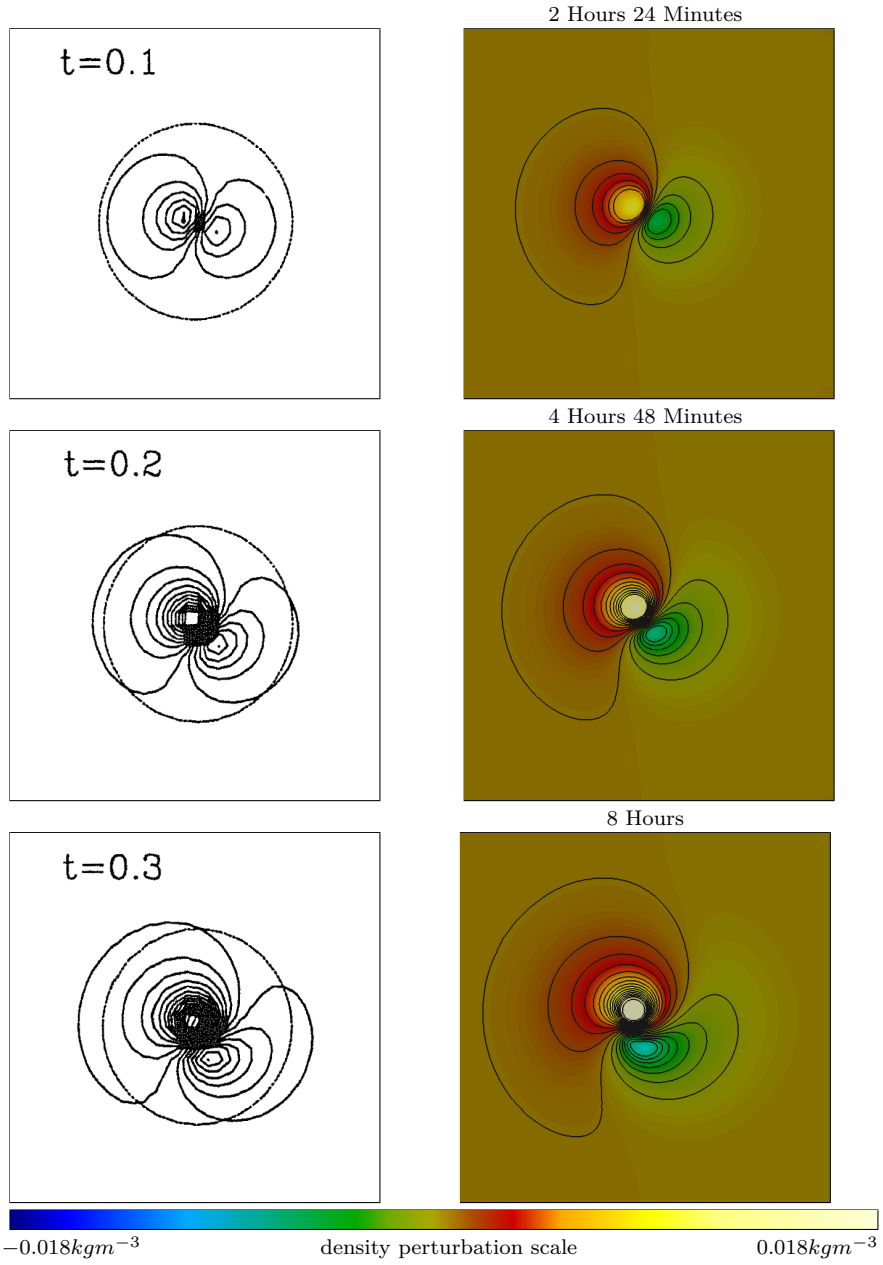

Fig. 7: Comparison of density perturbation field at 400 m depth with results obtained by Chapman and Haidvogel (1992), during the start-up of the calculations. The dashed circle in the reference data is the 4000 m isobath. For $t = 0.1$, isolines range from -0.0039 to 0.0051. For $t = 0.2$, isolines range from -0.0059 to 0.0101. For $t = 0.3$, isolines range from -0.0069 to 0.0161. Isolines interval is 0.001 $kg\ m^{-3}$. The same values are used for all panels.

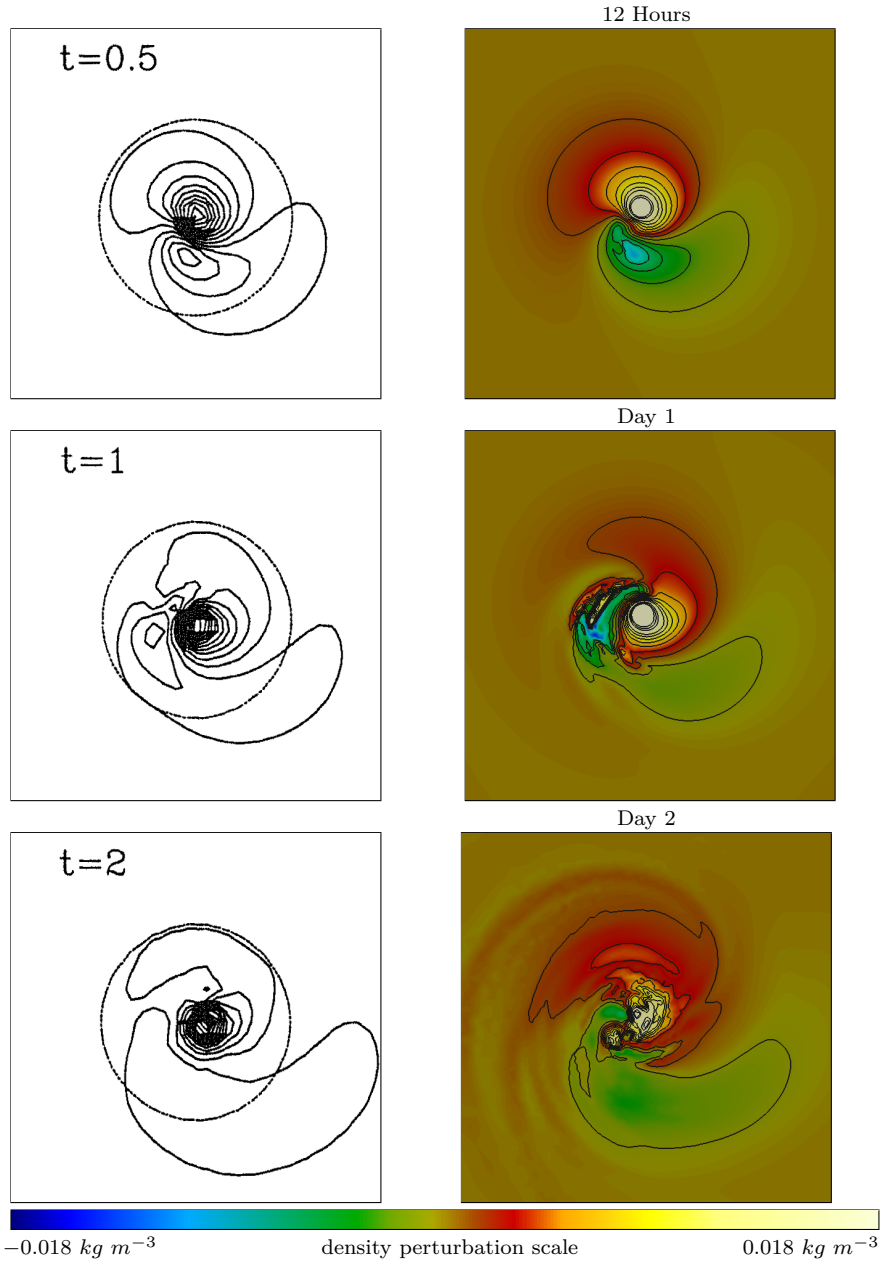

Fig. 8: Comparison of density perturbation field at 400 m depth with results obtained by Chapman and Haidvogel (1992) during the two first days. The dashed circle in the reference data is the 4000 m isobath. For $t = 0.5$, isolines range from -0.0069 to 0.0191. For $t = 1.0$, isolines range from -0.0049 to 0.0211. For $t = 2.0$, isolines range from -0.0009 to 0.0231. Isolines interval is 0.002 $kg\ m^{-3}$. The same values are used for all panels.

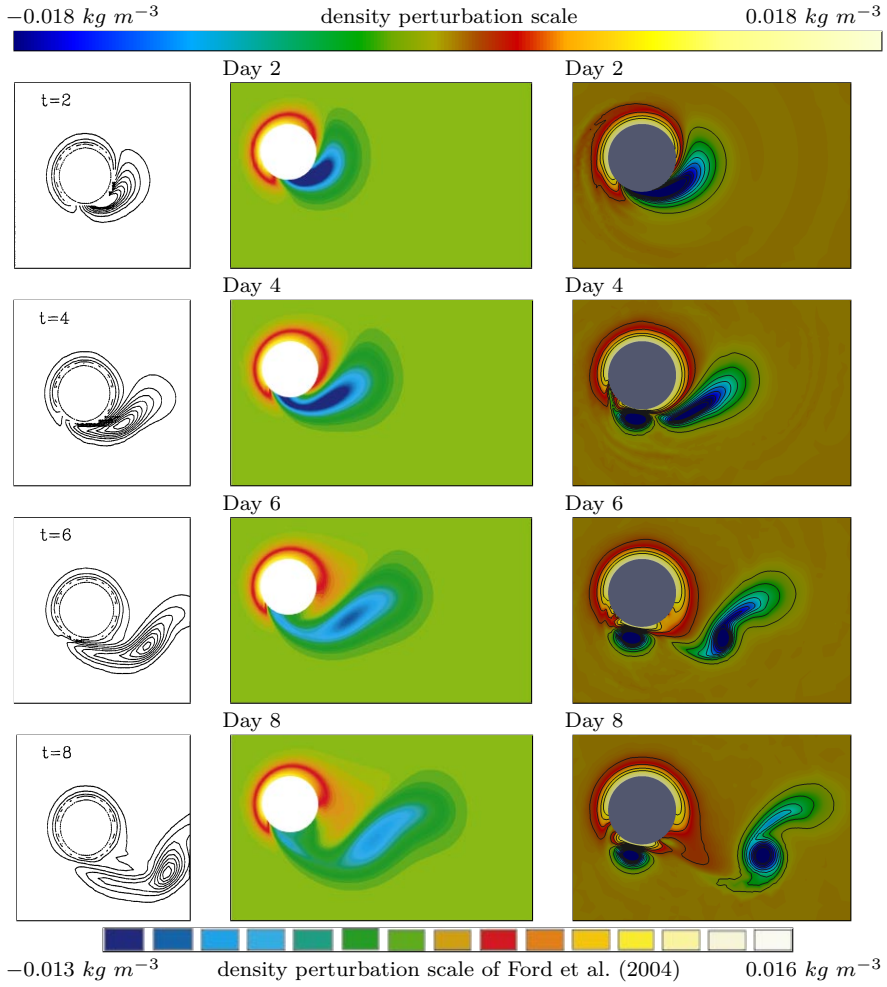

Fig. 9: Comparison of density perturbation field at 4000 m depth with results of Chapman and Haidvogel (1992) (left) and of Ford et al. (2004) (middle) during the first eight days. Isolevels are the same for the left and right sides, and range from -0.0212 to 0.0088 with a interval of 0.0025 $kg\ m^{-3}$.

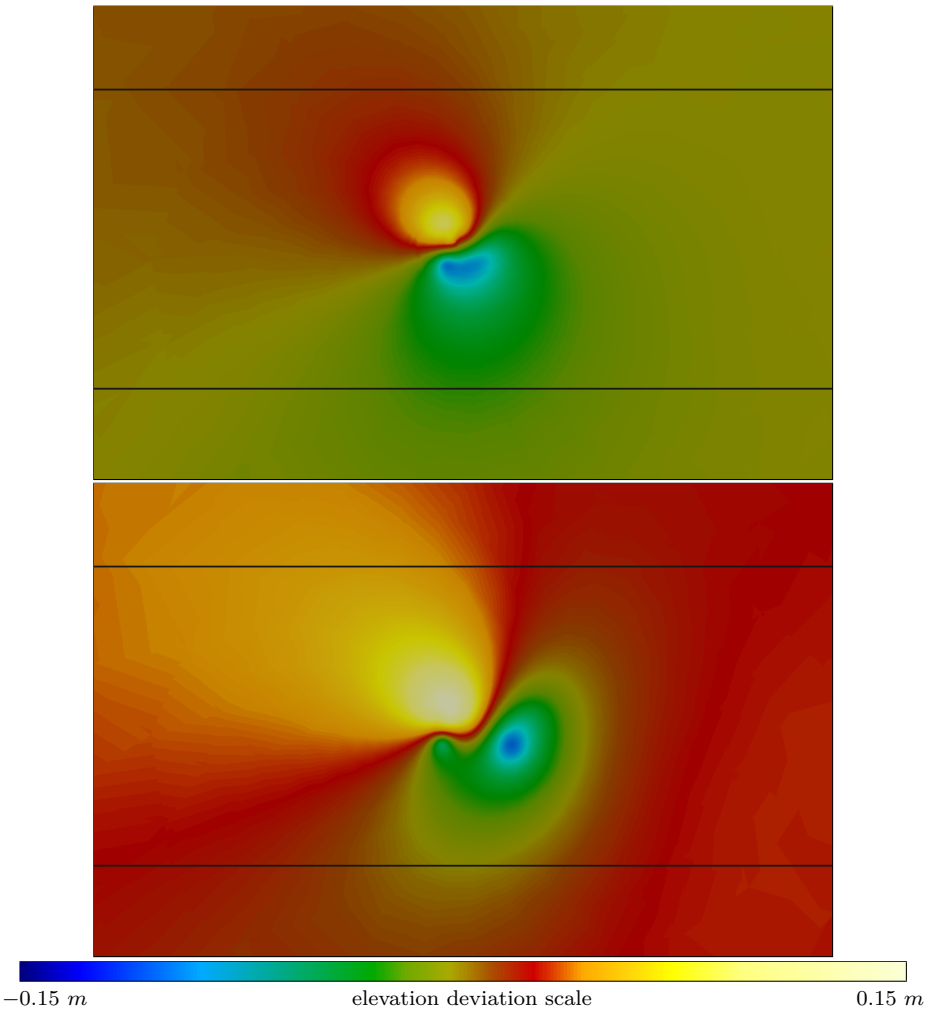

Fig. 10: Sea surface elevation deviation after three days (top) and seven days (bottom).. The black lines denotes the location of lateral boundary in Ford et al. (2004). It can be observed that the flow significantly varies outside of the domain denoted by the black lines.

7 Conclusions

An implicit-explicit time discretization for the three-dimensional free-surface baroclinic marine model described in Blaise et al. (2010) is proposed. The major contribution consists in the definition of a new implicit mode-splitting procedure with compatible barotropic and baroclinic problems. To achieve this, the two-dimensional barotropic problem is discretely obtained from the three-dimensional baroclinic problem. Compatibility between the two modes is enforced in a weak way by introducing Lagrange multipliers. The transports in the two- and three-dimensional problems are constrained by explicitly incorporating this compatibility constraint in the three-dimensional horizontal momentum equation. Combined with implicit-explicit Runge-Kutta (IMEX) methods, such an approach sounds very attractive. The order of accuracy can be selected as required. On the one hand, we take advantage of the stability of the implicit method that will damp the unresolved or poorly resolved modes. On the other hand, we could also benefit from the Total Variation Diminishing property of the explicit part of some methods.

Revisiting the benchmark flow over an isolated seamount of Blaise et al. (2010), we simulate the complex spiral wave dynamics that previous calculations were not able to capture, either because of the rigid-lid assumption or their numerical methods. Thanks to the unstructured nature of the mesh, the resolution is refined in the lee of the seamount, enabling a detailed representation of the wave dynamics in this region. Further, vortex shedding is observed. The early stages of the simulation compare well with the two previous calculations.

For such an implicit-explicit approach to be interesting, the discrete operators for the dynamics handled implicitly must be significantly stiffer than those for the explicit dynamics. Indeed, the time-step allowed by the IMEX scheme must be significantly larger than the time-step of a purely explicit discretization. It is definitely the case when the vertical mixing parameters are deduced from a turbulence closure. For the simulation of the internal waves in the lee of a moderately tall seamount, it is not really the case as the stratification is rather strong. The internal waves are fast, and the vertical viscosity is still reasonable. The time steps are only 20 times larger than the explicit time step, and are much more expensive, as local linear systems are solved. In our opinion, the way to faster computations is twofold. On one hand, the computation of the discrete terms can still be improved, by recasting most of the operations into efficient matrix-matrix products computed with highly optimized linear algebra subroutines. It is the classical optimization procedure of a numerical model. On the other hand, the time-stepping strategy can itself be improved. Indeed, most ocean models have resorted to a mode splitting approach to avoid solving three-dimensional linear systems. It may be necessary to go beyond this paradigm and investigate a full implicit approach. To be efficient, it must be scalable. Multigrid methods have the potential to provide scalable solutions to large-scale discrete problems. Further such multigrid methods do not need the matrix of the linear system to be assembled, significantly reducing the memory footprint of the algorithm. However, the design of an efficient multigrid algorithm is in itself a whole domain of research and goes much beyond the scope of this work.

Acknowledgments

Sébastien Blaise and Jonathan Lambrechts are Research fellows with the Belgian Fund for Research in Industry and Agriculture (FRIA). Richard Comblen is a Research fellow with the Belgian National Fund for Scientific Research (FNRS). Eric Deleersnijder is a Research associate with the Belgian National Fund for Scientific Research (FNRS). The research was conducted within the framework of the Interuniversity Attraction Pole TIMOTHY (IAP 6.13), funded by the Belgian Science Policy (BELSPO), and the programme ARC 04/09-316, funded by the Communauté Française de Belgique.

References

Adcroft, A., Hill, C., Marshall, J., 1997. Representation of topography by shaved cells in a height coordinate ocean model. Monthly Weather Review 95, 2293–2315.

Ascher, U. M., Ruuth, S. J., Spiteri, R. J., 1997. Implicit-explicit Runge-Kutta methods for time-dependent partial differential equations. Applied Numerical Mathematics 25, 151–167.

Ascher, U. M., Ruuth, S. J., Wetton, B. T., 1995. Implicit-explicit methods for time-dependent partial differential equations. SIAM Journal on Numerical Analysis 32, 797–823.

Blaise, S., Comblen, R., Legat, V., Remacle, J.-F., Deleersnijder, E., Lambrechts, J., 2010. A discontinuous finite element baroclinic marine model on unstructured prismatic meshes. Part I: space discretization. Ocean Dynamics (submitted).

Blumberg, A. F., Mellor, G. L., 1987. A description of three-dimensional coastal ocean circulation model. In: Heaps, N. S. (Ed.), Three Dimensional Coastal Ocean Model. American Geophysical Union, pp. 1–16.

Bryan, K., 1969. A numerical method for the study of the circulation of the world ocean. Journal of Computational Physics 4, 347–376.

Chapman, D. C., Haidvogel, D. B., 1992. Formation of Taylor caps over a tall isolated seamount in a stratified ocean. Geophysical and Astronomical Fluid Dynamics 64, 31–65.

Chapman, D. C., Haidvogel, D. B., 1993. Generation of internal lee waves trapped over a tall isolated seamount. Geophysical and Astronomical Fluid Dynamics 69, 33–54.

Chevaugeon, N., Hillewaert, K., Gallez, X., Ploumhans, P., Remacle, J.-F., 2007. Optimal numerical parametrization of discontinuous Galerkin method applied to wave propagation problems. Journal of Computational Physics 223, 188–207.

Cockburn, B., Shu, C.-W., september 2001. Runge-Kutta discontinuous Galerkin methods for convection-dominated problems. Journal of Scientific Computing 16, 173–261.

Cushman-Roisin, B., 1994. Introduction to Geophysical Fluid Dynamics. Prenctice Hall.

Deleersnijder, E., 1993. Numerical mass conservation in a free-surface sigma coordinate marine mode with mode splitting. Journal of Marine Systems 4, 365–370.

Dukowicz, J. K., Smith, R. D., April 1994. Implicit free-surface method for the Bryan-Cox-Semtner ocean model. Journal of Geophysical Research 99, 7991–8014.

Dukowicz, J. K., Smith, R. D., Malone, R. C., 1993. A reformulation and implementation of the Bryan-Cox-Semtner ocean model on the connection machine. Journal of Atmospheric and Oceanic Technology 10, 195–208.

Ezer, T., 2005. Entrainment, diapycnal mixing and transport in three-dimensional bottom gravity current simulations using the Mellor-Yamada turbulence closure. Ocean Modelling 9, 151–168.

Ezer, T., 2006. Topographic influence on overflow dynamics: Idealized numerical simulations of the Faroe Bank Channel overflow. Journal of Geophysical Research 111.

Ezer, T., Mellor, G. L., 2004. A generalized coordinate ocean model and a comparison of the bottom boundary layer dynamics in terrain-following and in z-level grids. Ocean Modelling 6, 379–403.

Ford, R., Pain, C.C., Piggott, M., Goddard, A., de Oliveira, C.R., Umpleby, A., 2004. A non-hydrostatic finite element model for three-dimensional stratified oceanic flows, Part II: Model validation. Monthly Weather Review 132, 2832–2844.

Giraldo, F. X., Perot, J. B., Fischer, P. F., 2003. A spectral element semi-lagrangian (SESL) method for the spherical shallow water equations. Journal of Computational Physics 190, 623–650.

Griffies, S. M., Böning, C., Bryan, F. O., Chassignet, E. P., Gerdes, R., Hasumi, H., Hirst, A., Treguier, A.-M., Webb, D., 2000. Developments in ocean climate modeling. Ocean Modelling 2, 123–192.

Hallberg, R., 1997. Stable split time stepping schemes for large-scale ocean modeling. Journal of Computational Physics 135, 54–56.

Higdon, R. L., de Szoeke, R. A., 1997. Barotropic-baroclinic time splitting for ocean circulation modeling. Journal of Computational Physics 135, 30–53.

Huppert, H. E., Bryan, K., 1976. Topographically generated eddies. Deep-Sea Research 23, 655–679.

Johnson, E. R., 1984. Starting flow for an obstable moving transversely in a rapidly rotating fluid. Journal of Fluid Mechanics 149, 71–88.

Killworth, P. D., Stainforth, D., Webb, D. J., Paterson, S. M., september 1991. The development of a free-surface Bryan-Cox-Semtner ocean model. Journal of Physical Oceanography 21, 1333–1348.

Kubatko, E., Dawson, C., Westerink, J., 2008. Time step restrictions for runge-kutta discontinuous galerkin methods on triangular grids. Journal of Computational Physics 227, 9697–9710.

Legg, S., Hallberg, R. W., Girton, J. B., 2006. Comparison of entrainment in overflows simulated by z-coordinate, isopycnal and non-hydrostatic models. Ocean Modelling 11, 69–97.

Marshall, J.C., Adcroft, A.J., Hill, C.N., Perelman, L., Heisey, C., 1997. A finite-volume, incompressible Navier Stokes model for studies of the ocean on parallel computers. Journal of Geophysical Research 102, 5753–5766.

Özgökmen, T. M., Chassignet, E. P., 2002. Dynamics of two-dimensional turbulent bottom gravity currents. Journal of Physical Oceanography 32, 1460–1478.

Tseng, Y.-H., Dietrich, D. E., 2006. Entrainment and transport in idealized three-dimensional gravity current simulation. Journal Of Atmospheric and Oceanic Technology 23, 1249–1269.

Verron, J., Le Provost, C., 1985. A numerical study of quasi-geostrophic flow over isolated topography. Journal of Fluid Mechanics 154, 231–252.

Wang, Q., 2007. The finite element ocean model and its aspect of vertical discretization. Ph.D. thesis, Bremen University.

Wang, Q., Danilov, S., Schröter, J., 2008a. Comparison of overflow simulations on different vertical grids using the finite element ocean circulation model. Ocean Modelling 20, 313–335.

Wang, Q., Danilov, S., Schröter, J., 2008b. Finite element ocean circulation model based on triangular prismatic elements, with application in studying the effect of topography representation. Journal of Geophysical Research 113.

White, L., Legat, V., Deleersnijder, E., 2008. Tracer conservation for three-dimensional, finite-element, free-surface, ocean modeling on moving prismatic meshes. Monthly Weather Review 136, 420–442.

Williamson, D. L., Drake, J. B., Hack, J. J., Jakob, R., Swarztrauber, P. N., 1992. A standard test set for numerical approximations to the shallow water equations in spherical geometry. Journal of Computational Physics 102, 211–224.